

Local Electrodynamics of a Disordered Conductor Model System Measured with a Microwave Impedance Microscope

Holger Thierschmann^{1,*}, Hale Cetinay^{2,3}, Matvey Finkel¹, Allard J. Katan¹, Marc P. Westig¹, Piet Van Mieghem², and Teun M. Klapwijk^{1,4}

¹*Kavli Institute of NanoScience, Delft University of Technology, Lorentzweg 1, 2628 CJ Delft, Netherlands*

²*Faculty of Electrical Engineering, Mathematics and Computer Science, Delft University of Technology, Mekelweg 4, 2628 CD Delft, The Netherlands*

³*Institute of Environmental Sciences, Faculty of Science, Leiden University, Einsteinweg 2, 2333 CC Leiden, Netherlands*

⁴*Physics Department, Moscow State Pedagogical University, Moscow 119991, Russia*

 (Received 26 August 2019; revised manuscript received 11 October 2019; published 22 January 2020)

We study the electrodynamic impedance of percolating conductors with a predefined network topology using a scanning microwave impedance microscope at gigahertz frequencies. For a given percolation number we observe strong spatial variations across a sample that correlate with the connected regions (clusters) in the network when the resistivity is low such as in aluminum. For the more-resistive material (Nb,Ti)N, the impedance becomes dominated by the local structure of the percolating network (connectivity). The results can be qualitatively understood and reproduced with a network current-spreading model based on the pseudoinverse Laplacian of the underlying network graph.

DOI: [10.1103/PhysRevApplied.13.014039](https://doi.org/10.1103/PhysRevApplied.13.014039)

I. INTRODUCTION

A large class of challenging problems in condensed-matter physics emerge from spatially inhomogeneous, coexisting electronic phases and percolation phenomena [1–3]. These include superconductor-insulator transitions [4], phase transitions in strongly correlated materials [5], and many properties observed in quantum materials [6,7]. To better address these problems, it is advantageous to have experimental access to the electronic properties on a local scale. Since conventional transport experiments measure the electrical properties on a global scale, scanning-near-field-imaging techniques have emerged as key experimental tools [1,8–14]. These techniques use high-frequency signals that are scattered off or reflected from a sharp metallic probe, and provide quantitative information on the electric and dielectric properties of the sample material in the vicinity of the probe tip. In this manner the electrodynamic response can be studied even for electrically disconnected, small conductive patches in an insulating environment, without the need for external electrical contacts and a fully conducting path through the sample [5,9,10,12,15,16]. Significant progress has been made toward a quantitative interpretation of the signal [14,17–20]. However, an important question remains as

to how short-range and long-range structural correlations of different electronic phases, arising inherently in electrically inhomogeneous materials, modify the electrodynamic response. Studying such contributions from disorder in an experiment is difficult because the spatial details during a phase transition typically follow seemingly random distributions and thus cannot be known *a priori*.

Here we address through experiments and calculations the local impedance of conductors that exhibit a precisely known spatial distribution of disorder. We design and realize a set of microscopic two-dimensional percolated networks from different metallic materials using lithography techniques. The networks serve as model systems for a disordered conductor that exhibits an insulator-to-metal transition (IMT). To measure the electrodynamic impedance locally, we use a room-temperature scanning microwave impedance microscope (SMIM). We find that the impedance is strongly affected by the local topology of the disordered network as well as by the resistivity of the material.

II. EXPERIMENT

The SMIM used for our experiments is based on an Asylum Cypher atomic force microscope with a Prime-Nano Scanwave extension. The SMIM uses a shielded cantilever as depicted in Fig. 1(a) to guide a microwave tone to the metallic tip, where the signal is reflected back into the cantilever transmission line and fed into a

*hthiersch@gmail.com

microwave readout circuit [10,17]. When the tip (typical apex diameter approximately 100 nm) is far from the sample, an impedance-matching circuit and a common-mode cancellation loop suppress signal reflection. As the tip is landed and scanned over a sample, the local material properties in the vicinity of the probe modify the generally complex-numbered tip impedance Z [Fig. 1(a)], giving rise to changes in the real and imaginary components of the reflected microwave signal. The disordered conductor model systems are patterned on a 100-nm-thick dielectric SiO_2 layer (with relative permittivity $\epsilon_r = 3.9$) that covers a conductive Si substrate. The impedance Z is therefore described in a lumped-element circuit in which the substrate acts as a ground plane. The circuit consists of a series network of two capacitors C_{tip} and C_{sub} , representing the coupling between the tip and the sample and between the sample and the substrate, respectively. A resistor R_s takes

into account resistive losses inside the network. Hence

$$Z = R_s + \frac{1}{i2\pi f} \left(\frac{1}{C_{\text{tip}}} + \frac{1}{C_{\text{sub}}} \right), \quad (1)$$

with f being the applied frequency (3 GHz). The real and imaginary components of the reflected signal are demodulated in the microwave readout circuit into two dc signals, which correspond to the resistive component (SMIMRe) and the capacitive component (SMIMIm) of the tip-sample admittance $Y = Z^{-1}$. The SMIM signal allows analysis of material properties because R_s , C_{tip} , and C_{sub} are affected on a microscopic level by the electrical conductivity σ of the conductive patch underneath the tip. Therefore, the SMIMIm and SMIMRe signals are coupled. When σ changes homogeneously, one obtains characteristic curves for SMIMIm and SMIMRe as sketched in the right inset in Fig. 1(a). SMIMIm exhibits a transition from low signal to high signal as σ increases, while SMIMRe approaches 0 at both extremes and exhibits a peak in between.

We are interested in the SMIM response for an inhomogeneous sample. Therefore, we design a conductor model system consisting of a set of nanostructured metallic two-dimensional bond-percolated networks. We aim to probe the impedance with spatial resolution higher than the scale of disorder and to study spatial variations across the sample as a result of the disordered electrodynamic landscape. Therefore, we design each network to consist of a 50×50 square grid of nominally $200 \times 200 \text{ nm}^2$, metallic squares, which we refer to as “sites.” In comparison, the apex diameter of the SMIM tip is on the order of 100 nm. Hence, the SMIM signal can be assigned to the particular site underneath the tip [21]. Each site can be connected with its four nearest neighbors by $100 \times 200 \text{ nm}^2$ metallic bonds. Disorder is introduced by randomly placing only a fraction of bonds in the network. In this fashion, the IMT is modeled by a series of patterns for which the number of bonds increases. Each pattern is then characterized by the total fraction of bonds p . The fully insulating state corresponds to an entirely disconnected network with no bonds, $p = 0$. For the fully metallic state, $p = 1$. When $0 < p < 1$, clusters of connected sites form, giving rise to a highly disordered pattern as displayed for the case $p = 0.5$ in Fig. 1(b) and in the enlargement in Fig. 1(c). Each cluster can be characterized by its mass m , given by the number of connected sites in that cluster. For small p , the clusters consist of only a few sites, and hence the mean cluster mass m and the mass of the largest cluster m_{max} for a given p are small [see Fig. 1(d)]. As p is increased, the clusters grow and eventually merge with their neighbors. The IMT coincides with the emergence of the so-called spanning cluster at a critical percolation number p_c . Here, m_{max} is sufficiently large to establish a continuous conductive path across the whole network, rendering the previously insulating system a conductor at the

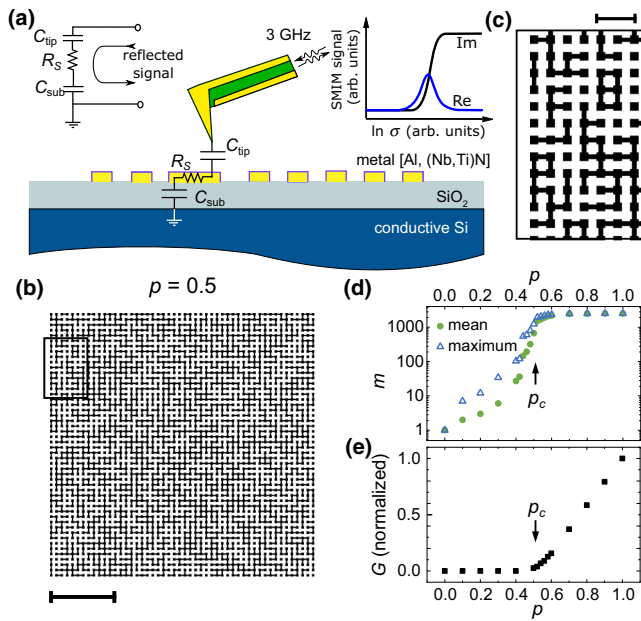


FIG. 1. (a) Scanning microwave impedance microscopy: a 3-GHz signal is launched to a transmission-line cantilever and is reflected due to near-field interactions at the tip. The near-field interactions can be described in a lumped-element circuit (left inset) consisting of capacitors C_{tip} and C_{sub} and a resistor R_s . The characteristic SMIM response curve for the imaginary part and the real part of the reflected signal are coupled through the sample conductivity σ (right inset). (b) Bond-percolated network pattern for a disordered conductor model system with percolation number $p = 0.5$. Scale bar $5 \mu\text{m}$. (c) Enlarged view of the region of the network indicated by the frame in (b). Scale bar $1 \mu\text{m}$. (d) Mean cluster mass m_{mean} and mass of the largest cluster m_{max} calculated for each network pattern versus p . (e) Calculated dc conductance G between the left edge and the right edge of the networks versus p , normalized to $G(p = 1)$. p_c indicates the IMT.

global scale. This is directly reflected in the conductance G , as calculated for each p [22] between the left edge and the right edge [see Fig. 1(e) and Ref. [21]], which becomes nonzero at $p_c = 0.5$, as expected from percolation theory for a two-dimensional square network [21,23].

We fabricate the set of patterns from two different materials with different resistivity. This allows us to study the local impedance for a wider range of parameters. As a low-resistivity material we choose a 25-nm aluminum (Al) thin film with sheet resistance $R_{\text{sheet}}^{\text{Al}} = 1.04 \Omega/\square$, patterned with standard lift-off techniques. As a high-resistivity material, we use sputtered, 10 nm-thick (Nb,Ti)N [24], with $R_{\text{sheet}}^{(\text{Nb,Ti})\text{N}} = 10.2 \text{ k}\Omega/\square$.

All experiments reported here are performed in contact mode.

III. RESULTS

A. Aluminum networks

Figure 2 shows typical SMIM images obtained for the network made of Al with $p = 0.5$. The data are normalized with respect to a reference sample [21] and they are nulled with respect to the SiO_2 dielectric layer. Figure 2(a) shows the imaginary component SMIMIm, corresponding to capacitive contributions to the impedance. In Fig. 2(b) we show the real part, SMIMRe, representing the Ohmic contributions. Both images reveal a structure that is different from the underlying network depicted in Fig. 1(a). Figure 2 shows that SMIMIm (i.e., the capacitance) is large (bright) over large areas, while only smaller patches show a small response (dark). SMIMRe indicates that Ohmic resistance contributes to the impedance in only a few, smaller regions. Since the pattern was fabricated from a single Al film the observed spatial variations can not be explained with changes in the local conductivity of the Al. We attribute the difference to disorder and thus to the formation of clusters in a network with nontrivial topology.

Figure 2(c) depicts the network underlying the SMIM data [see Fig. 1(a)]; however, we have removed all sites and bonds from this pattern, except the clusters with the largest cluster mass m , labeled 1–4. The resulting shape emerging from these clusters strongly resembles the image in Fig. 2(a). This suggests a correlation between the capacitive impedance (SMIMIm) and the cluster mass m . We further observe that areas with a strong SMIMRe signal coincide with clusters 2, 3, and 4. The connection between cluster mass m and impedance appears to hold also for smaller m . It can be inferred from the enlarged view of SMIMIm and SMIMRe in Figs. 2(d) and 2(e), where we have added the underlying network pattern from Fig. 1(c) as a guide for the eye. Within a cluster the SMIM signals appear to be uniform. We can therefore calculate the mean signal obtained for each cluster and assign the result to the corresponding m . This is shown in Figs. 2(f) and 2(g) for an arbitrary set of clusters, obtained from various Al patterns of different p . Figure 2(f) reveals a monotonous

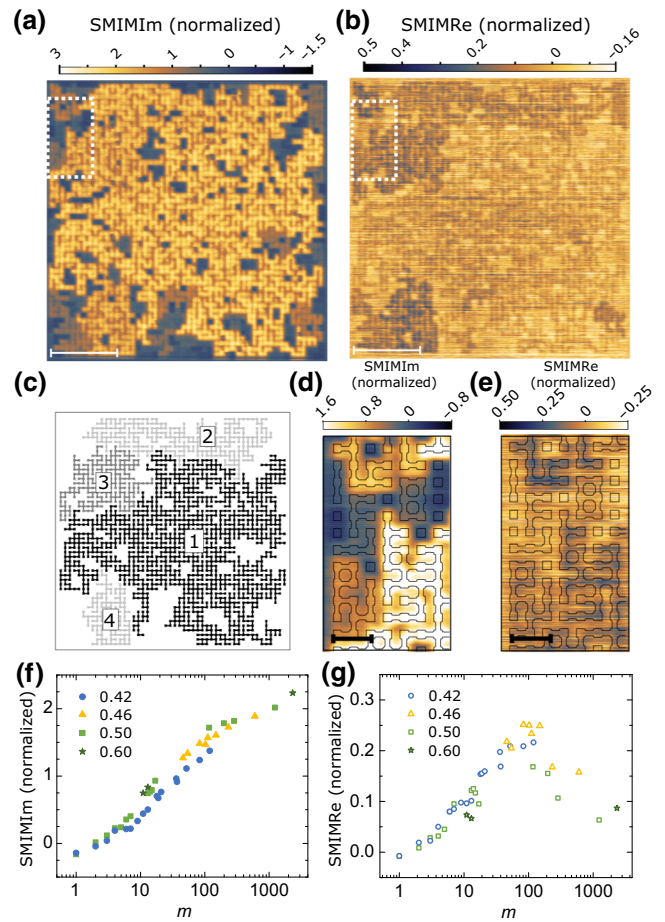


FIG. 2. (a) SMIMIm image and (b) SMIMRe image of the conductor model system realized from aluminum with $p = 0.5$. The underlying network is identical with the pattern depicted in Fig. 1(b). Scale bar $5 \mu\text{m}$. (c) Network pattern for $p = 0.5$ with all clusters removed except for the four largest ones, labeled 1–4. (d) Enlargement of SMIMIm image and (e) enlargement of SMIMRe image in the region indicated in (a),(b) with a white frame. As a guide for the eye, the underlying pattern has been added to the images. Scale bar $1 \mu\text{m}$. (f) Mean SMIMIm signal and (g) mean SMIMRe signal of various clusters versus cluster mass m . The data are obtained from Al samples with $p = 0.42, 0.46, 0.5, \text{ and } 0.6$.

increase with m for SMIMIm. The maximum slope occurs approximately around $m = 100$. In contrast, SMIMRe in Fig. 2(g) exhibits a peak here, while it decreases toward 0 for smaller m and approaches a small, but nonzero value toward $m = 2500$.

B. (Nb,Ti)N networks

When the exact same network pattern is made from a less-conductive material, the corresponding SMIM images change drastically. This is shown in Fig. 3, where the network was realized from (Nb,Ti)N. SMIMIm [Fig. 3(a)] reveals a highly nonuniform distribution of the imaginary impedance that does not bear a clear resemblance with

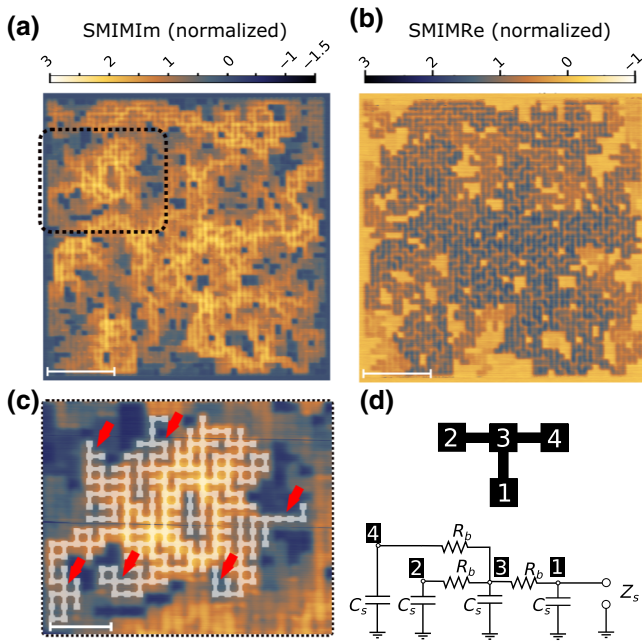


FIG. 3. (a) SMIMIm response and (b) SMIMRe response of the pattern realized from (Nb,Ti)N with $p = 0.5$. Scale bar $5 \mu\text{m}$. (c) Enlarged view of SMIMIm response of cluster 3, indicated with a frame in (a). The geometry of cluster 3 is indicated in gray. The color scale is the same as in (a). Red arrows indicate polyps of the cluster with low connectivity, yielding low signal. Scale bar $2 \mu\text{m}$. (d) Impedance-network model used to calculate the sample impedance Z_s for a cluster with $m = 4$ with the tip at site 1. C_s denotes the capacitance of a site to substrate ground, and R_b corresponds to the resistance of a bond connection.

the clusters in Fig. 2(c). Instead, a backbone-type structure becomes visible. SMIMRe [Fig. 3(b)], in contrast, does not show a backbone structure. Here the cluster delimitation can be inferred more clearly. However, signal variations within the clusters are significant, which renders an analysis as done for Al in Fig. 2 with SMIMIm and SMIMRe as a function of cluster mass m not applicable. In Fig. 3(c) we therefore directly compare SMIMIm with the underlying network topology for the region of cluster 3 [see Fig. 2(c)]. We observe that the capacitance (SMIMIm) is small at the outside branches and polyps of the cluster. It becomes large toward the inside, in particular in a well-connected, ring-shaped region, circling the cluster's center.

SMIMIm images of the IMT around p_c are displayed in Fig. 4(a) for Al (top row) and (Nb,Ti)N (bottom row), highlighting the evolution of the local impedance as structural correlations and network topology evolve.

IV. DISCUSSION AND MODEL

We can understand the observations for the local impedance within the lumped-element picture introduced in Fig. 1(a) by taking into account the electrodynamic environment of the scanning-probe experiment and the detailed

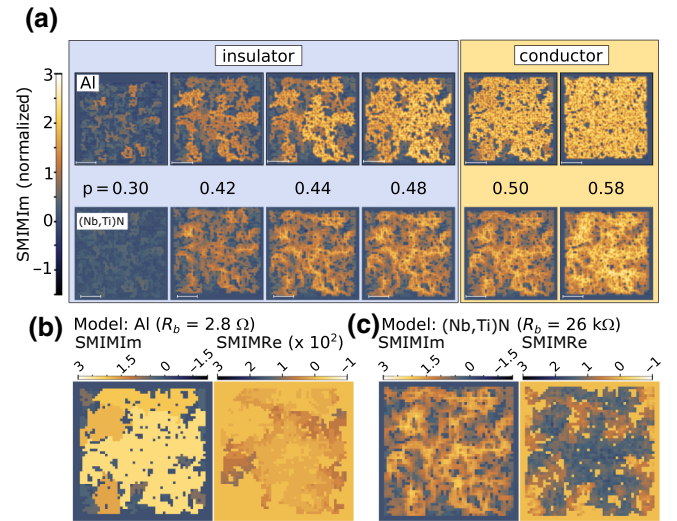


FIG. 4. (a) Experimental SMIMIm images for Al (top row) and (Nb,Ti)N (bottom row) for various percolation numbers p from the globally insulating state (blue background) to the conductive state (yellow background). (b),(c) Model calculations of the SMIMIm response and the SMIMRe response of the network with $p = 0.5$ for Al and (Nb,Ti)N, respectively, obtained with an impedance-network model [21]. Note that the SMIMRe response in (b) is scaled by a factor of 10^2 .

disordered-network pattern. We replace the resistor R_s and the capacitor C_{sub} in Eq. 1 by an impedance network that reflects the network topology and the capacitive coupling at each site to the substrate ground plane. Figure 3(d) displays such a network for a small cluster with $m = 4$, with the probe tip positioned at site 1. Each bond connection is represented by a resistor R_b . Each site is taken into account by a capacitor C_s to the substrate.

When R_b is small compared with the impedance of a single site to ground $Z_{C_s} = (i2\pi f C_s)^{-1}$, the microwave currents injected at the probe tip can spread easily across the whole cluster. This applies for Al, where $R_b = 2.8 \Omega$, while $Z_{C_s} \approx 1.4 \text{ M}\Omega \gg R_b$ (with $C_s = 4 \times 10^{-2} \text{ fF}$ [21]). As a result, all site capacitors C_s of a cluster contribute approximately equally to the total capacitance C_{sub} , such that $C_{\text{sub}} \approx m C_s$. This explains the absence of variations within a cluster as well as the observed scaling of the capacitive impedance, SMIMIm, with m . However, when R_b becomes sufficiently large, as is the case for (Nb,Ti)N ($R_b = 26 \text{ k}\Omega$), current spreading is impeded. Capacitive contributions to the total impedance, therefore, get suppressed when the sites are connected through only a high-resistance current path (e.g., via several bonds in series). This is the case at the polyps and dead ends in cluster 3 in Fig. 3(c) (arrows). Here the impedance is large due to a small total capacitance C_{sub} . In contrast, in regions where the local connectivity is high, for instance toward the center ring of cluster 3, current injected at the tip can spread

over a large number of sites through many parallel current paths. This leads to a smaller impedance due to a large capacitance, and thus to a high SMIMIm signal. In this picture, the impedance at a particular site reflects the local connectivity of the network, giving rise to the observed backbone-type structure.

The RC-network picture indicates how the capacitance to the substrate ground plane C_{sub} may serve as a tuning knob for the range of contrast in a scanning-microwave-impedance-microscopy experiment. Modifying the thickness and permittivity of the dielectric will shift the quantitatively sensitive SMIM response to smaller or larger patches of film (i.e., to different scales of disorder).

On the basis of the RC-network approach, we use a network current-spreading model and the pseudoinverse Laplacian of the underlying network graph [22] to compute the impedance Z at each site and, using Eq. 1, to compare it with the experimental data [21]. The results are shown in Figs. 4(b) and 4(c) for Al and (Nb,Ti)N, respectively. The computed SMIMIm images reproduce the experimental data [see Figs. 2(a) and 3(a)] very well. The computed SMIMRe signal [see Figs. 2(b) and 3(b)], however, deviates more from the experiments. While for (Nb,Ti)N the deviations are small and occur mainly in samples with larger p [21], the deviations are particularly large for Al, where the SMIMRe signal, compared with the corresponding SMIMIm signal, is orders of magnitude smaller than in the experiments. The differences between the model prediction and the data on Al therefore suggest that the simple RC-network model used here is incomplete.

The present experiments highlight the electrodynamic environment of the tip provided by the inhomogeneous sample. It is reminiscent of the importance of the electrodynamic environment in scanning tunneling experiments, such as in a Josephson-current-based tunneling experiment (see, e.g., Ref. [25]). Here the metallic tip of the scanning probe acts as a resonant antenna interacting with the Josephson oscillations. Our experiments indicate that for electrically inhomogeneous materials, such as a structured film of Al or disordered superconductors such as (Nb,Ti)N, TiN, or InO [26,27], the sample under study also contributes to the effective electrodynamic environment.

Finally, we note that it may be an interesting route in the future to explore techniques to invert the procedure described here (i.e., to construct the underlying disordered network in an unknown material from a SMIM image).

V. CONCLUSION

We study experimentally the role of disorder for the local impedance in a percolating conductor model system using microwave impedance microscopy. We find that structural properties such as cluster size, network topology, and local connectivity can significantly influence the local

electrodynamic environment, depending on the material resistivity and the degree of disorder in the system.

ACKNOWLEDGMENTS

We thank David J. Thoen for help with the (Nb,Ti)N sample fabrication. We acknowledge funding through European Research Council Advanced Grant No. 339306 (METIQUM).

-
- [1] D. N. Basov, R. D. Averitt, D. Van der Marel, M. Dressel, and K. Haule, Electrostatics of correlated electron materials, *Rev. Mod. Phys.* **83**, 471 (2011).
 - [2] S. Kirkpatrick, Percolation and conduction, *Rev. Mod. Phys.* **45**, 574 (1973).
 - [3] P. Van Mieghem, Theory of band tails in heavily doped semiconductors, *Rev. Mod. Phys.* **64**, 755 (1992).
 - [4] V. F. Gantmakher and V. T. Dolgoplov, Superconductor-insulator quantum phase transition, *Phys. Usp.* **53**, 1 (2010).
 - [5] M. M. Qazilbash, M. Brehm, B.-G. Chae, P.-C. Ho, G. O. Andreev, B.-J. Kim, S. J. Yun, A. Balatsky, M. Maple, and F. Keilmann *et al.*, Mott transition in VO_2 revealed by infrared spectroscopy and nano-imaging, *Science* **318**, 1750 (2007).
 - [6] B. Keimer and J. Moore, The physics of quantum materials, *Nat. Phys.* **13**, 1045 (2017).
 - [7] A. Soumyanarayanan, N. Reyren, A. Fert, and C. Panagopoulos, Emergent phenomena induced by spin-orbit coupling at surfaces and interfaces, *Nature* **539**, 509 (2016).
 - [8] B. T. Rosner and D. W. Van Der Weide, High-frequency near-field microscopy, *Rev. Sci. Instrum.* **73**, 2505 (2002).
 - [9] A. J. Huber, F. Keilmann, J. Wittborn, J. Aizpurua, and R. Hillenbrand, Terahertz near-field nanoscopy of mobile carriers in single semiconductor nanodevices, *Nano Lett.* **8**, 3766 (2008).
 - [10] K. Lai, M. Nakamura, W. Kundhikanjana, M. Kawasaki, Y. Tokura, M. A. Kelly, and Z.-X. Shen, Mesoscopic percolating resistance network in a strained manganite thin film, *Science* **329**, 190 (2010).
 - [11] E. Y. Ma, M. R. Calvo, J. Wang, B. Lian, M. Mühlbauer, C. Brüne, Y.-T. Cui, K. Lai, W. Kundhikanjana, and Y. Yang *et al.*, Unexpected edge conduction in mercury telluride quantum wells under broken time-reversal symmetry, *Nat. Commun.* **6**, 7252 (2015).
 - [12] G. Gramse, A. Kölker, T. Lim, T. J. Stock, H. Solanki, S. R. Schofield, E. Brinciotti, G. Aeppli, F. Kienberger, and N. J. Curson, Nondestructive imaging of atomically thin nanostructures buried in silicon, *Sci. Adv.* **3**, e1602586 (2017).
 - [13] J. M. Atkin, S. Berweger, A. C. Jones, and M. B. Raschke, Nano-optical imaging and spectroscopy of order, phases, and domains in complex solids, *Adv. Phys.* **61**, 745 (2012).
 - [14] S. M. Anlage, V. V. Talanov, and A. R. Schwartz, in *Scanning Probe Microscopy* (Springer, New York, 2007), p. 215.
 - [15] E. Y. Ma, Y.-T. Cui, K. Ueda, S. Tang, K. Chen, N. Tamura, P. M. Wu, J. Fujioka, Y. Tokura, and Z.-X. Shen,

- Mobile metallic domain walls in an all-in-all-out magnetic insulator, *Science* **350**, 538 (2015).
- [16] P. J. de Visser, R. Chua, J. O. Island, M. Finkel, A. J. Katan, H. Thierschmann, H. S. van der Zant, and T. M. Klapwijk, Spatial conductivity mapping of unprotected and capped black phosphorus using microwave microscopy, *2D Mater.* **3**, 021002 (2016).
- [17] K. Lai, W. Kundhikanjana, M. Kelly, and Z. Shen, Modeling and characterization of a cantilever-based near-field scanning microwave impedance microscope, *Rev. Sci. Instrum.* **79**, 063703 (2008).
- [18] H. Huber, I. Humer, M. Hochleitner, M. Fenner, M. Moertelmaier, C. Rankl, A. Imtiaz, T. Wallis, H. Tanbakuchi, and P. Hinterdorfer *et al.*, Calibrated nanoscale dopant profiling using a scanning microwave microscope, *J. Appl. Phys.* **111**, 014301 (2012).
- [19] G. Gramse, M. Kasper, L. Fumagalli, G. Gomila, P. Hinterdorfer, and F. Kienberger, Calibrated complex impedance and permittivity measurements with scanning microwave microscopy, *Nanotechnology* **25**, 145703 (2014).
- [20] A. Buchter, J. Hoffmann, A. Delvallée, E. Brinciotti, D. Hapiuk, C. Licitra, K. Louarn, A. Arnoult, G. Almuneau, and F. Piquemal *et al.*, Scanning microwave microscopy applied to semiconducting GaAs structures, *Rev. Sci. Instrum.* **89**, 023704 (2018).
- [21] See Supplemental Material at <http://link.aps.org/supplemental/10.1103/PhysRevApplied.13.014039> for detailed information on experimental procedures, model calculations, and extended experimental and modeling data.
- [22] P. Van Mieghem, K. Devriendt, and H. Cetinay, Pseudoinverse of the laplacian and best spreader node in a network, *Phys. Rev. E* **96**, 032311 (2017).
- [23] D. Stauffer, Scaling theory of percolation clusters, *Phys. Rep.* **54**, 1 (1979).
- [24] D. J. Thoen, B. G. C. Bos, E. Haalebos, T. Klapwijk, J. Baselmans, and A. Endo, Superconducting nbtin thin films with highly uniform properties over a \varnothing 100 mm wafer, *IEEE Trans. Appl. Supercond.* **27**, 1 (2016).
- [25] C. R. Ast, B. Jäck, J. Senkpiel, M. Eltschka, M. Etzkorn, J. Ankerhold, and K. Kern, Sensing the quantum limit in scanning tunnelling spectroscopy, *Nat. Commun.* **7**, 13009 (2016).
- [26] B. Sacépé, C. Chapelier, T. Baturina, V. Vinokur, M. Baklanov, and M. Sanquer, Disorder-induced Inhomogeneities of the Superconducting State Close to the Superconductor-insulator Transition, *Phys. Rev. Lett.* **101**, 157006 (2008).
- [27] T. Dubouchet, B. Sacépé, J. Seidemann, D. Shahar, M. Sanquer, and C. Chapelier, Collective energy gap of preformed cooper pairs in disordered superconductors, *Nat. Phys.* **15**, 233 (2019).

Supplementary Information: Local electrodynamics of a disordered conductor model system measured with a microwave impedance microscope

Holger Thierschmann,^{1,*} Hale Cetinay,^{2,3} Matvey Finkel,¹ Allard J. Katan,¹ Marc P. Westig,¹ Piet Van Mieghem,² and Teun M. Klapwijk^{1,4}

¹*Kavli Institute of NanoScience, Delft University of Technology,
Lorentzweg 1, 2628 CJ Delft, The Netherlands*

²*Faculty of Electrical Engineering, Delft University of Technology, Delft, The Netherlands*

³*Institute of Environmental Sciences, Faculty of Science,
Leiden University, Einsteinweg 2, 2333 CC Leiden, The Netherlands*

⁴*Physics Department, Moscow State Pedagogical University, Moscow 119991, Russia.*

(Dated: December 7, 2019)

SMIM REFERENCE SAMPLE

In order to be able to directly compare sMIM data obtained from different structures, we use a reference sample consisting of $5\ \mu\text{m} \times 5\ \mu\text{m}$ Al squares on SiO_2 , as provided by the sMIM manufacturer PrimeNano Inc (Fig. S1). While collecting the data from the NbTiN and Al networks, we frequently scanned the reference sample. This allows us to normalize the sMIM data for each network shown in the main text, with respect to the mean contrast in the sMIM-Im channel obtained from the reference sample. In this manner the sMIM data for different structures become comparable and signal changes due to tip wear-off or electronic drift get removed.

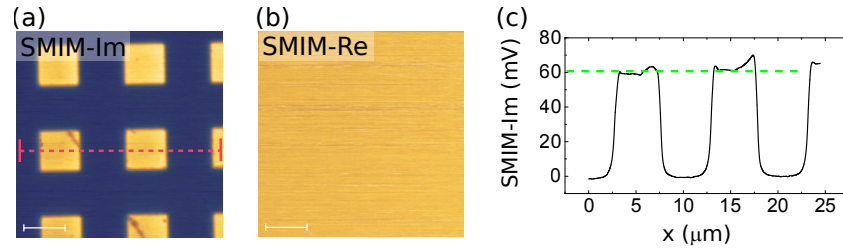


FIG. S1. (a) sMIM-Im and (b) sMIM-Re from a measurement of the calibration sample. Since the sample consists of highly conductive aluminum on a dielectric substrate, contrast is only visible in sMIM-Im while contrast is absent in sMIM-Re. The scale bar corresponds to $5\ \mu\text{m}$. (c) Cross section taken from (a). The sMIM-Im amplitude obtained for the Al squares (green dashed line) from frequently repeated scans of the reference sample is taken as a reference for the sMIM measurements shown in the main text.

TOPOGRAPHY CHARACTERIZATION OF NETWORKS

Figure S2 (a) and (b) depict topography line scans of two disconnected sites fabricated out of Aluminum and NbTiN, respectively. Note that these scans were taken with a different, sharper tip than the one used for the sMIM measurements. While the size of the NbTiN sites ($w_s \approx 230$ nm) is close to the nominal value (200 nm), the Al site is larger ($w_s \approx 260$ nm). This is a result of the different fabrication techniques, which consisted of a lift-off process for Al, and a dry-etch step for the NbTiN sample.

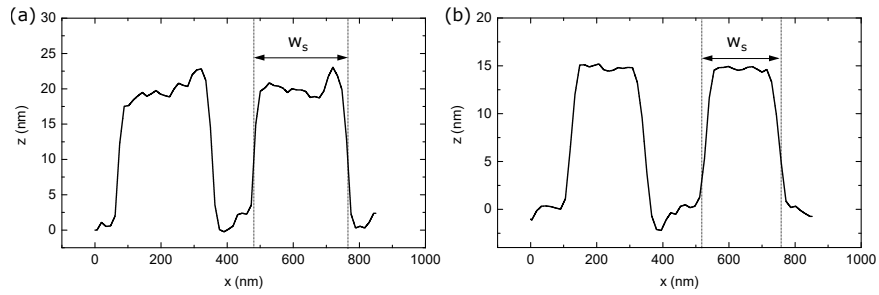


FIG. S2. Topography scans of two adjacent disconnected sites. **(a)** Aluminum. **(b)** NbTiN. The size of the sites is denoted with w_s . Note that these traces were taken with a different tip than the one used for the sMIM measurements.

CONTRIBUTIONS TO THE SMIM SIGNAL FROM NEIGHBORING SITES

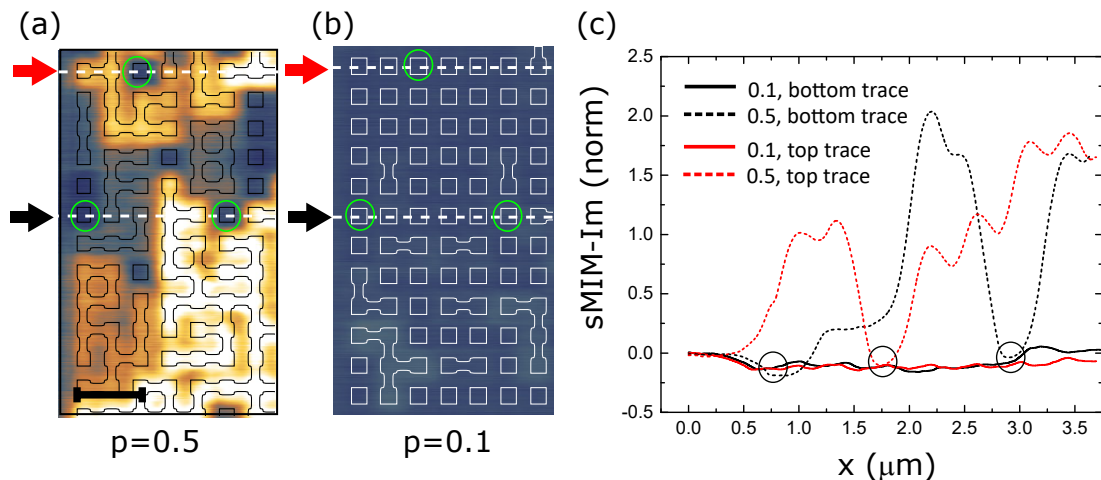


FIG. S3. **(a)** sMIM-Im for the Al sample with $p = 0.5$. Close up of the same region as shown in Fig. 2(d) in the main text. The circles indicate individual singlets that are surrounded by larger cluster. **(b)** sMIM-Im image of the same set of sites as in (a) for $p = 0.1$. Circles indicate the same sites as in (a), which are now surrounded by other singlets and small clusters. **(c)** Horizontal traces extracted from (a) (dashed lines) and (b) (solid lines), along the dotted lines indicated with a red (top) and black (bottom) arrow. Circles indicate the sMIM-Im signal at those locations marked with circles in (a) and (b). We find that despite strong differences in the environment of these sites, the difference in the sMIM-Im signal are barely visible. This confirms that the measured signal originates from the microwave current being injected only at a single site underneath the tip, justifying the current spreading model used for the calculations.

TIP SHAPE ESTIMATE

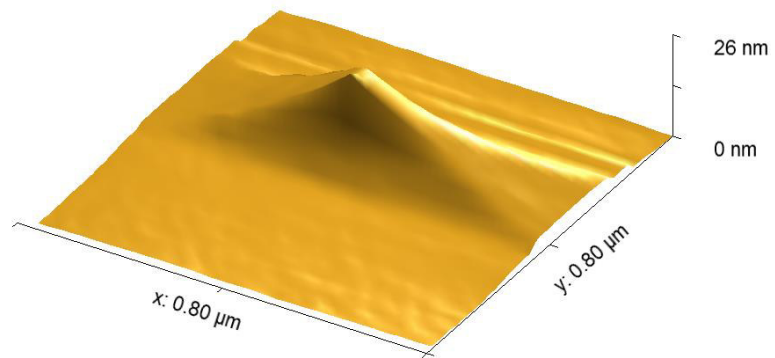


FIG. S4. We have used the *Gwyddion* blind tip shape estimate algorithm [1] based on the topography images to extract a quantitative estimate of the tip geometry.

DISORDERED CONDUCTOR MODEL SYSTEMS

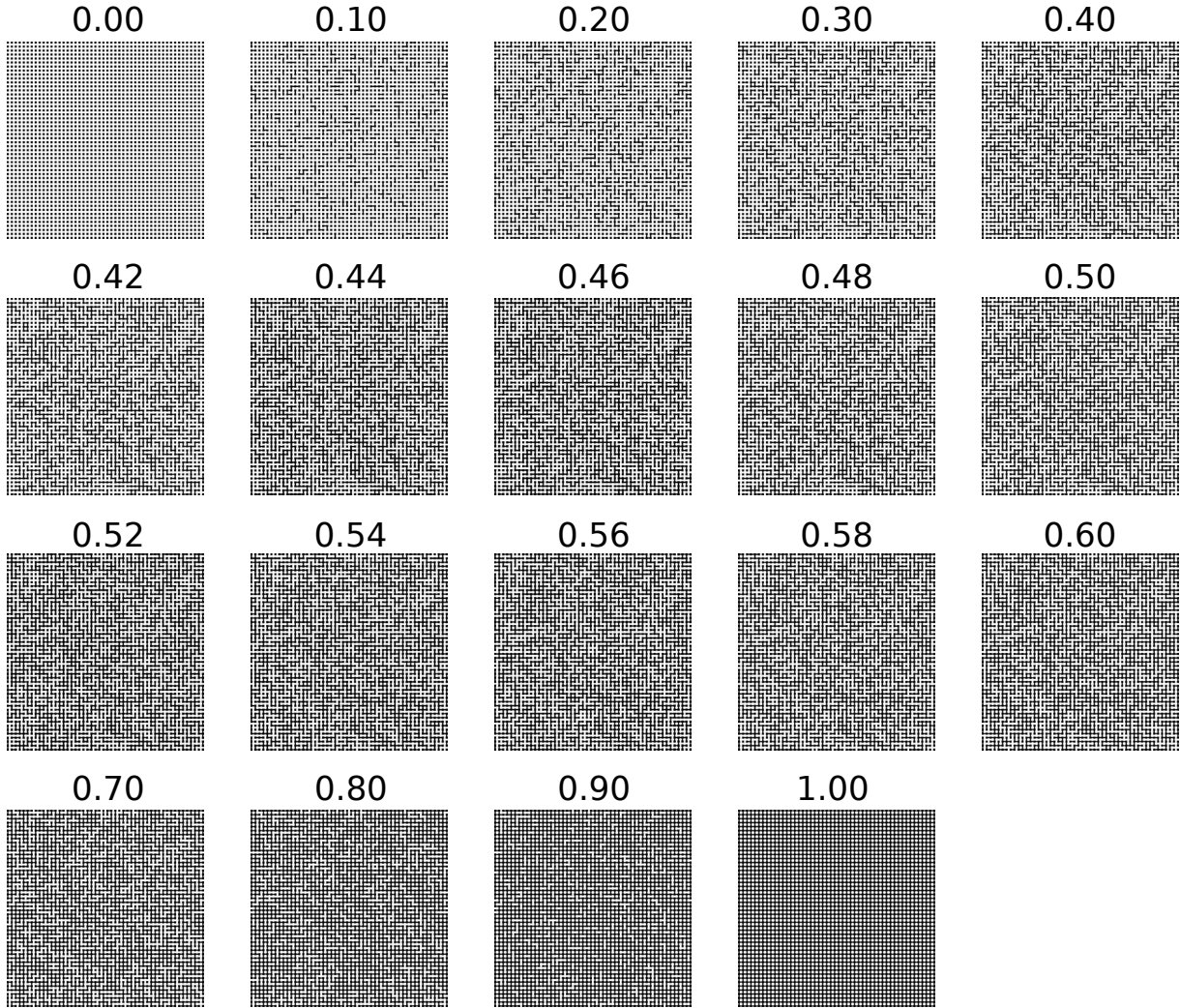


FIG. S5. Percolated network patterns used to realize the model systems for the insulator-metal-transition. The patterns consist of 50×50 sites (total number $N = 2500$). The numbers indicate the percolation number p , i.e. the fraction of occupied bonds (total number $N_b = 4900$) in the network. The patterns have been designed to be incremental, i.e. when increasing p for example from 0.1 to 0.2, the bond configuration for $p = 0.1$ is maintained and 10 % more bonds are added to the system.

CALCULATION OF MODEL PARAMETERS C_s , C_{tip} AND R_b

The capacitance between a single site and the substrate ground plane is calculated using a textbook closed-form expression for a microstrip line [2] (corresponding to a metallic plate above an infinite ground plane), with the goal to use a simple approximation that also takes into account stray fields,

$$C_s = \frac{\epsilon_r w_s [w_s/h + 1.393 + 0.667 \ln(w_s/h + 1.444)]}{120\pi c}, \quad (1)$$

with site dimensions $w_s = 250$ nm (estimated from the topography images), dielectric thickness $h = 100$ nm, the dielectric constant $\epsilon_r = 3.9$ and the vacuum speed of light c . This yields $C_s = 4 \times 10^{-2}$ fF.

The tip-site capacitance C_{tip} is calculated in a similar fashion. From the topography images obtained along with the sMIM data, we infer that the sMIM tip is strongly worn down (cf. blind tip estimate in Fig. S4). We empirically find good agreement for $C_{\text{tip}} = 4$ fF, corresponding, in a parallel plate capacitor model, to a tip size of 200 nm interacting capacitively with the sample, and 1 nm thin layer of natural Al_2O_3 covering the Al structures ($\epsilon_r = 10$).

Using this value to model the experiments on NbTiN also yields good agreement. This is surprising since obviously these structures are not expected to exhibit an Al_2O_3 layer. However, while little is known about the oxidation of NbTiN structures under ambient conditions, some studies suggest that a dielectric film is formed [3]. In our case, even though dielectric constant and thickness of such a film are likely to be different compared to the Al samples, apparently the resulting C_{tip} is of similar order.

The resistance of each bond, R_b , is calculated using the measured sheet resistance ($R_{\text{sheet}}^{\text{Al}} = 1.04 \Omega/\square$, $R_{\text{sheet}}^{\text{NbTiN}} = 10.2 \text{ k}\Omega/\square$) and the geometry of the bond connection $w_b = 100$ nm and $l_b = 200$ nm. Including the resistance of half a site on each side of the bond connection adds R_{sheet} to the bond resistance, $R_b = R_{\text{sheet}} \frac{l_b}{w_b} + R_{\text{sheet}}$. This yields $R_b^{\text{Al}} = 2.5 \Omega$ and $R_b^{\text{NbTiN}} = 26 \Omega$, as used in the main text.

IMPEDANCE NETWORK MODEL

In order to calculate the electrical properties of our disordered conductor model systems we follow an approach described by Van Mieghem et al. in Ref. [4]. We convert each of the percolated conductor patterns shown in fig. S5 into a matrix P and construct the corresponding weighted

adjacency matrix \tilde{A} , yielding an $N \times N$ matrix ($N = 2500$ being the total number of sites) which only has non-zero entries $q_{ij} = 1/R_b$ if the sites i and j are directly connected through a single bond in P . The capacitive connection to the substrate ground plane in the experiments is taken into account by adding a $(N + 1)^{th}$ ground node to \tilde{A} that is directly connected to every other site via the complex impedance $(i2\pi f C_s)^{-1}$. This yields the modified adjacency matrix \tilde{A}_{gnd} from which we can construct the Laplacian \tilde{Q}

$$\tilde{Q} = \text{diag} \left(\sum_{k=1}^{N+1} \tilde{A}_{\text{gnd},ik} \right) - \tilde{A}_{\text{gnd}}. \quad (2)$$

The complex effective impedance between the two nodes a and b is then given by [4]

$$Z_{s_{ab}} = Q_{aa}^\dagger + Q_{bb}^\dagger - 2Q_{ab}^\dagger, \quad (3)$$

where Q^\dagger is the pseudo-inverse of the weighted Laplacian \tilde{Q} .

The local impedance Z_s of the network at each site i , as relevant in our experiment, is then obtained by calculating the impedance between site i and the ground node, $Z_{s_{i,\text{gnd}}}$.

In addition to $Z_{s_{i,\text{gnd}}}$, signal reflection at the cantilever tip is also determined by the capacitive tip-site coupling, C_{tip} . Hence,

$$Z_i = Z_{s_{i,\text{gnd}}} + \frac{1}{i(2\pi f)C_{\text{tip}}}. \quad (4)$$

The dissipative and capacitive component of the measured sMIM signal as plotted in Fig. 4 (a) and (b) in the main text, sMIM-Im and sMIM-Re, are then obtained by taking the real and imaginary components of the total admittance $Y_i = Z_i^{-1}$ for each site i in the network.

The macroscopic conductance G between the left and the right edge of each pattern as plotted in Fig. 1(d) in the main text, is obtained by summing up the conductance between each site on the left edge and all the sites of the right edge. G is then given by the real component of the result. Since G corresponds to a dc conductance, we ensure that contributions from ac currents through the ground node are suppressed in this calculation by letting $C_s \rightarrow 0$.

COMPARISON

In this section we compare sMIM-Im results obtained on a percolating network for two different modes: contact mode (as used in the main article) and tapping mode. Figure S6(a) shows contact mode data from an aluminum pattern with $p = 0.5$. (Note that the network is a different one than that used in the main text.) Figures S6(c) and (d) display the underlying network and the regions covered by the 3 largest clusters, respectively. Comparison with fig. S6(a) confirms the correlation between large sMIM-Im signal and large cluster size, as discussed in the main text.

Figure S6(b) displays sMIM-Im data obtained in tapping mode at a tapping frequency $f = 81.7$ kHz and a tapping amplitude $a \approx 100$ nm. Through the mechanical oscillation of the cantilever the microwave signal gets modulated at the tapping frequency f and is detected with a Lock-In amplifier. The resulting image of the percolated network strongly resembles the results obtained in contact mode, suggesting that the scanning mode does not dramatically influence the results. We can see, however, that the signals differ in more subtle aspects. First, the signal between two adjacent sites does not reach the zero level (as on the SiO_2 dielectric) but remains at higher values, if the two sites are part of larger clusters. Second, the contrast between small and larger clusters is smaller in tapping mode. This can be inferred from Fig. S6(e) where we compare two traces extracted from Fig. S6(a) and (b) along the white dashed lines. The tapping data are plotted as a red, dashed line in Fig. S6(e), the contact mode data are shown as a black, solid line. The data have been scaled such that the signal on the left onset of the network at $x = 2$ mm corresponds to sMIM-Im magnitude 0.6. Here, contact and tapping mode yield similar sMIM-Im. Towards the right edge of the network, in the range $x = 14$ to 22 mm, the trace contains a series of individual, disconnected sites. We see that here the tapping mode signal appears to be slightly larger than the contact mode signal. This could indicate that in tapping mode contrast becomes reduced as the clusters become larger, thus shifting the sensitivity of sMIM towards smaller clusters and towards a more local scale.

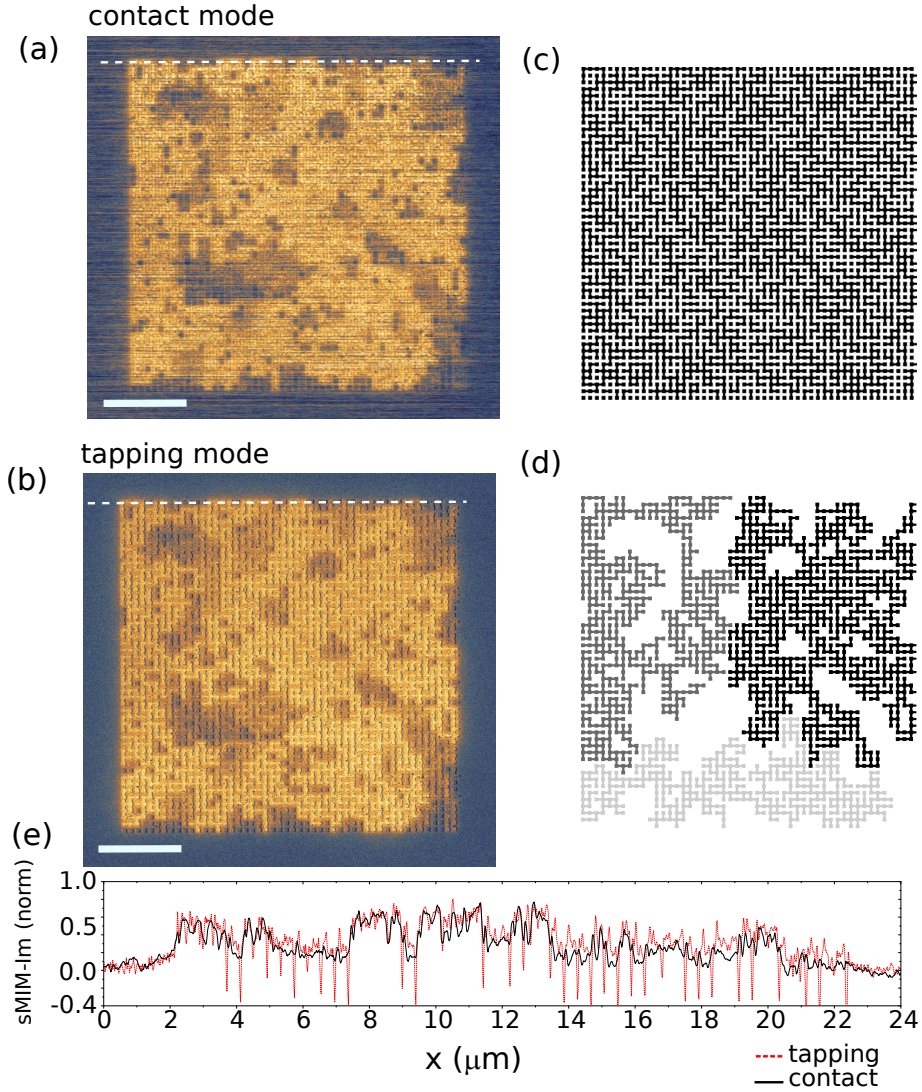


FIG. S6. **(a)** Contact mode sMIM-Im data from a network made from 25 nm Al with $p = 0.5$ (Note that this is a different pattern than the one used in the main text.) **(b)** Same network as in (a), measured in tapping mode (tapping amplitude $a \approx 100$ nm.) The scale bar corresponds to $5 \mu\text{m}$. **(c)** Network topology underlying the images in (a) and (b). **(d)** Three largest clusters of the network in (c). **(e)** Line traces extracted from (a) and (b) along the white dashed lines. Red, dashed: tapping mode. Black, solid: contact mode.

ADDITIONAL SMIM DATA

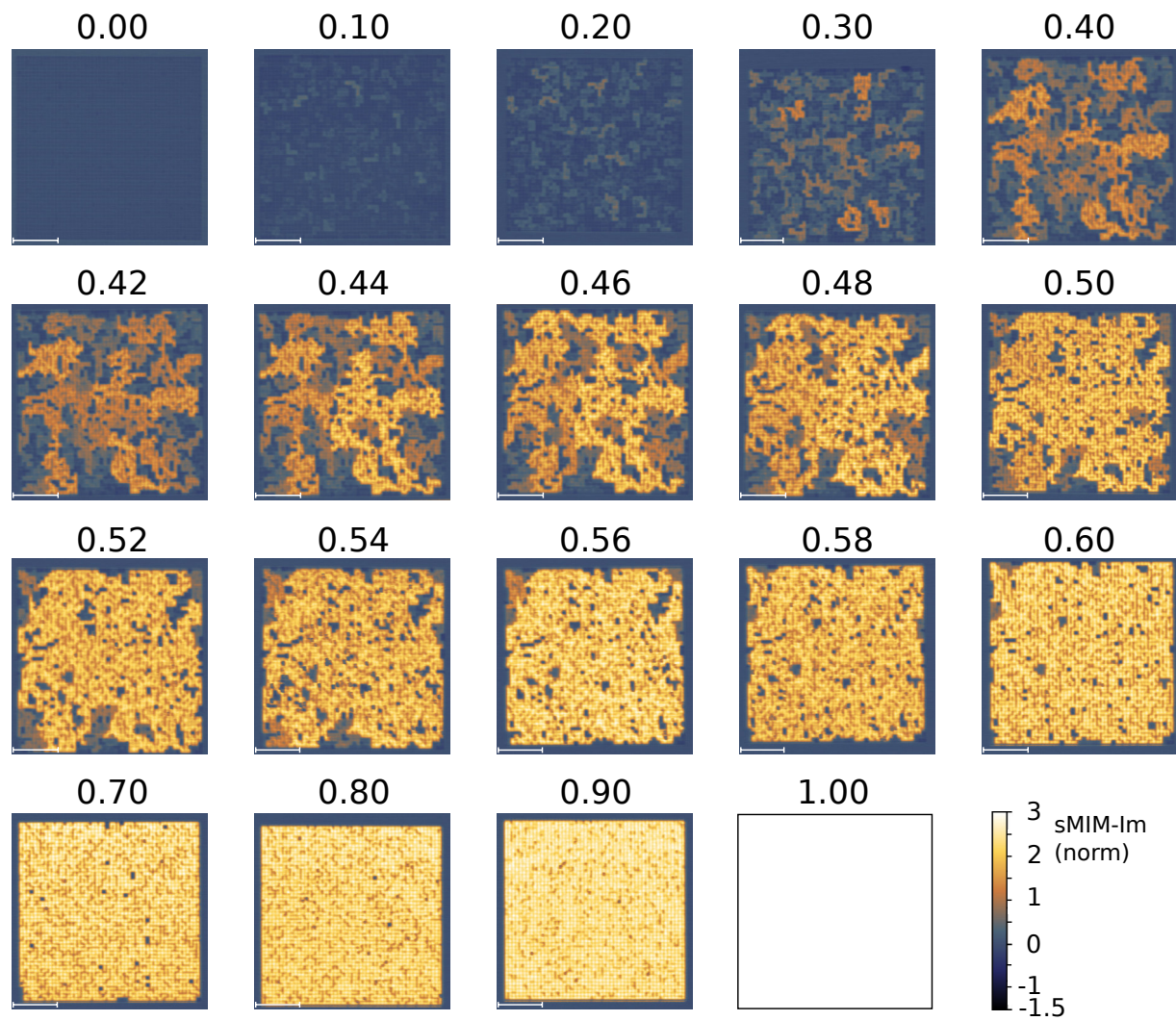


FIG. S7. Aluminum- sMIM-Im: Experimental data

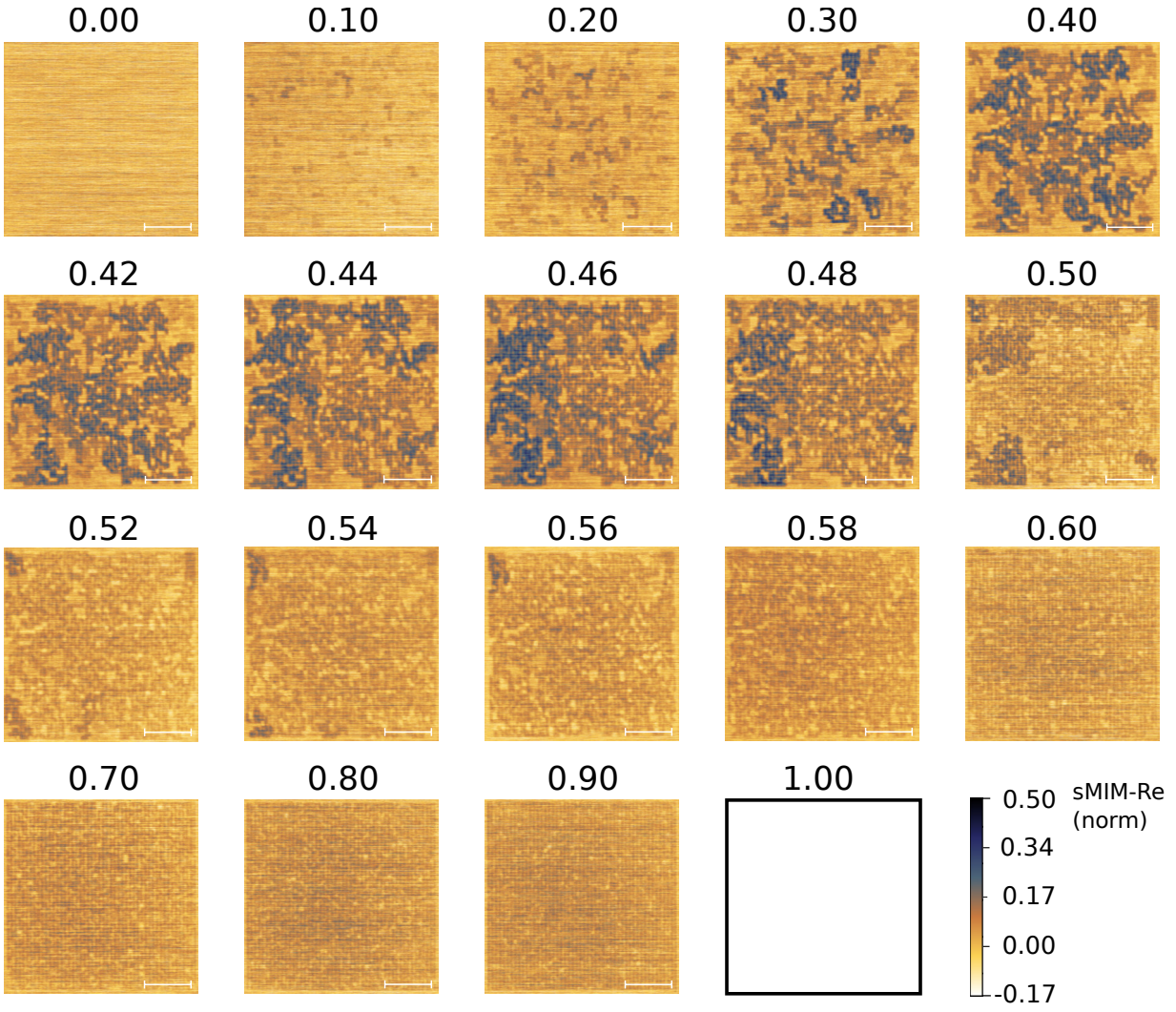


FIG. S8. Aluminum - sMIM-Re: Experimental data

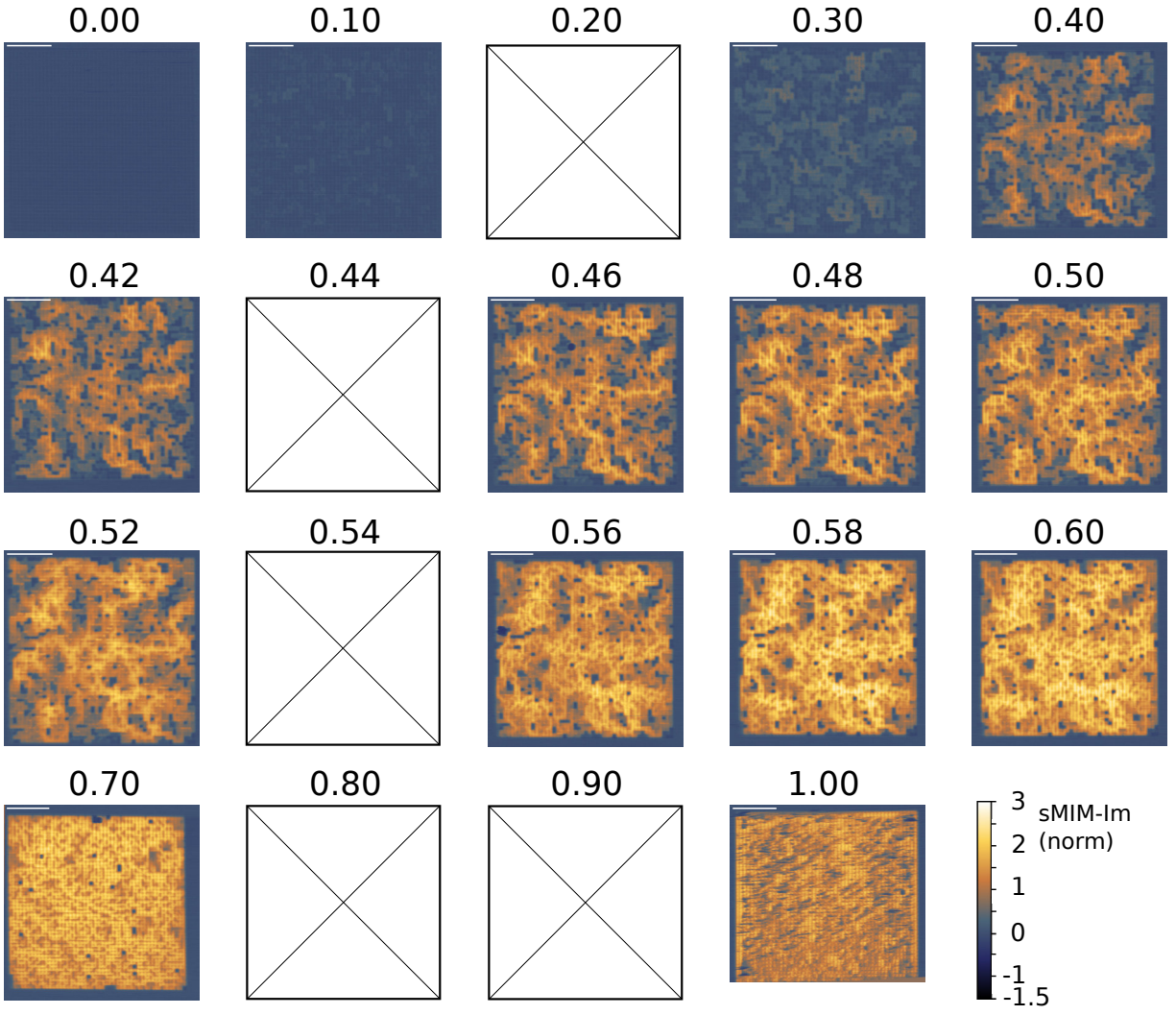


FIG. S9. **NbTiN - sMIM-Im: Experimental data.** Fields marked with a cross could not be measured because the fabricated structures were damaged. For $p = 1$, parts of the sample were covered with dirt residues from the sample fabrication, which appear as darker streaks in the image.

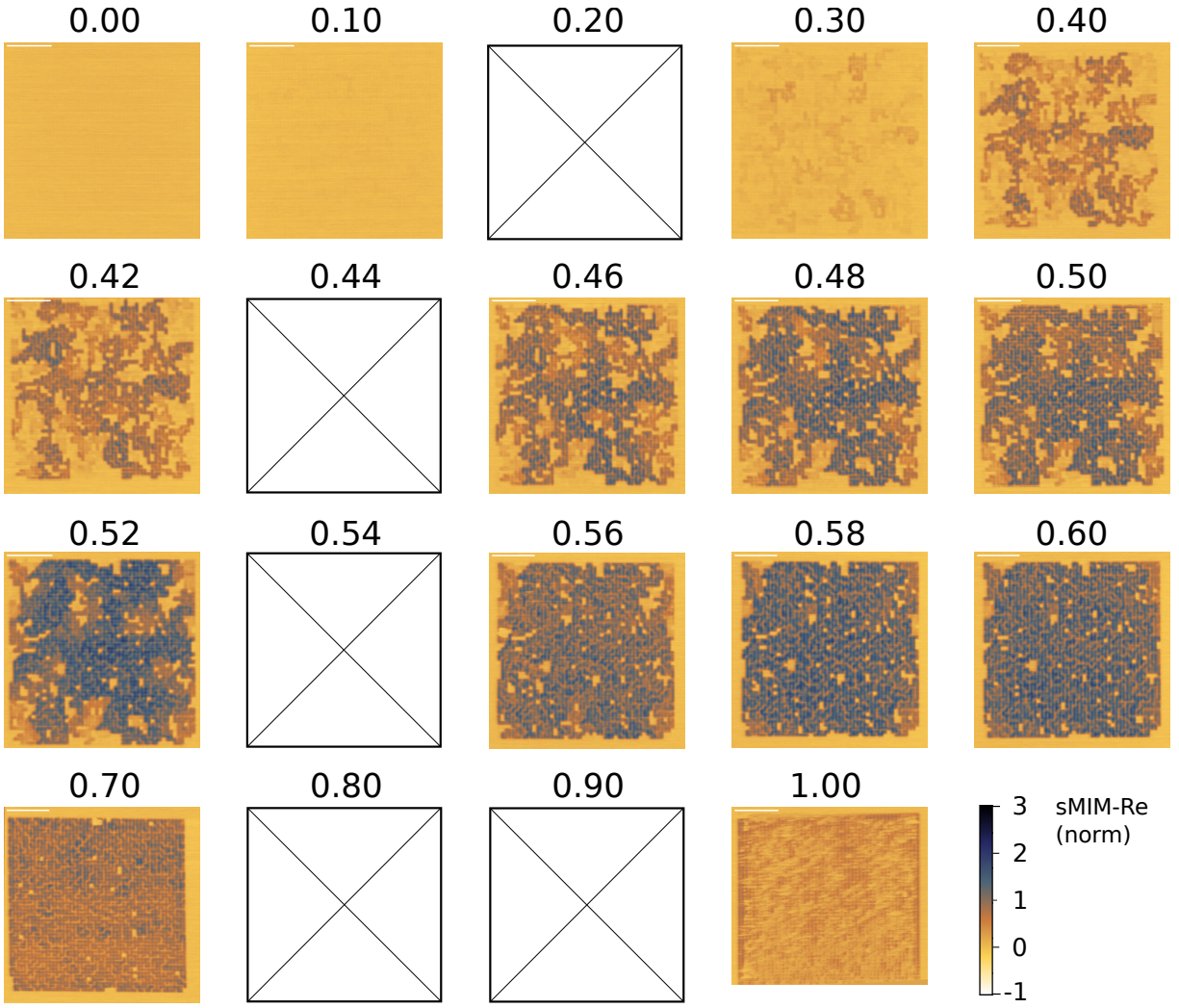


FIG. S10. **NbTiN - sMIM-Re: Experimental data.** Fields marked with a cross could not be measured because the fabricated structures were damaged. For $p = 1$, parts of the sample are covered with dirt residues from the sample fabrication. Here dissipation is reduced, leading to a suppressed sMIM-Re signal.

RESULTS OF THE NETWORK MODEL CALCULATION

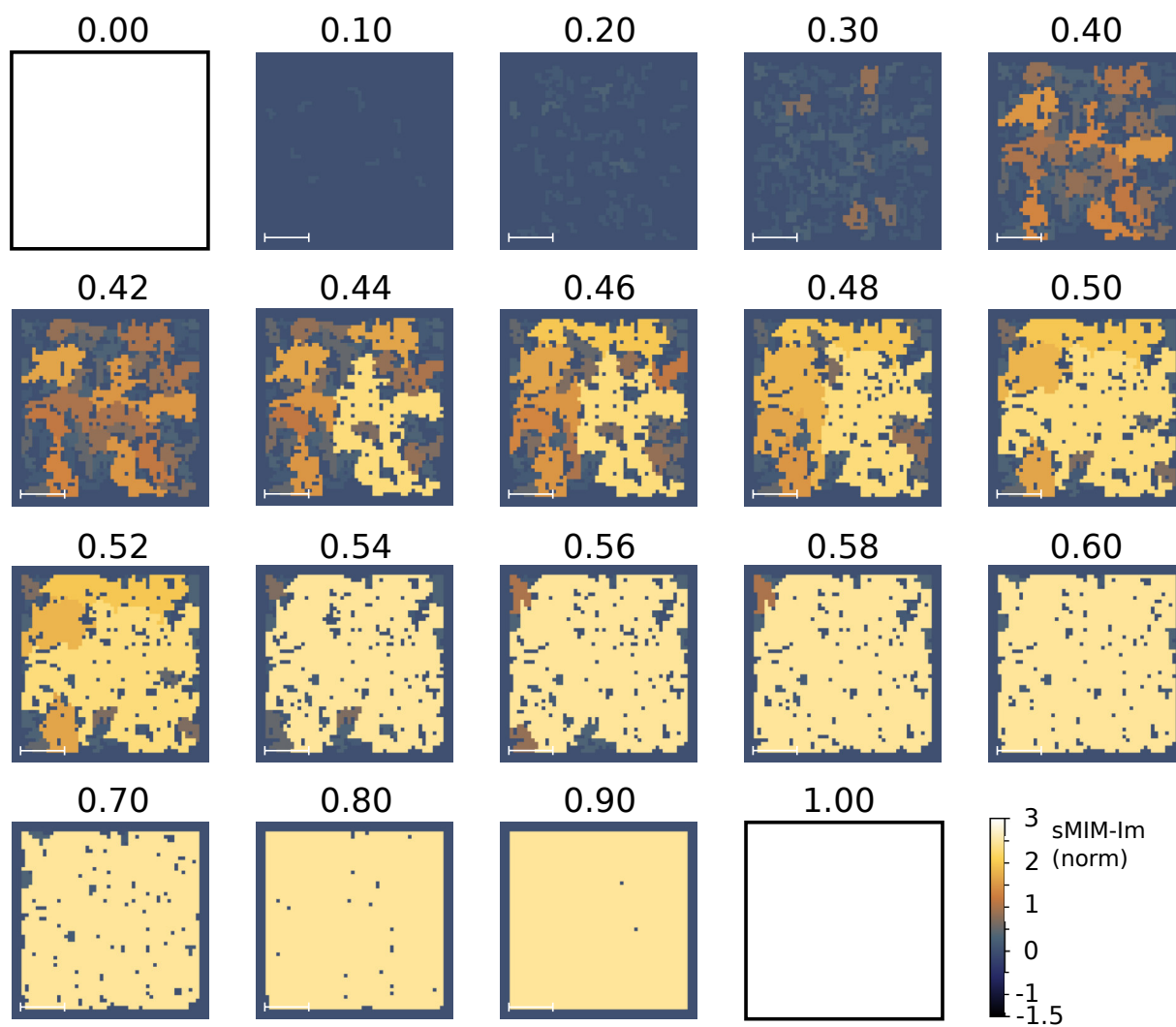


FIG. S11. Aluminum- sMIM-Im: Model calculations.

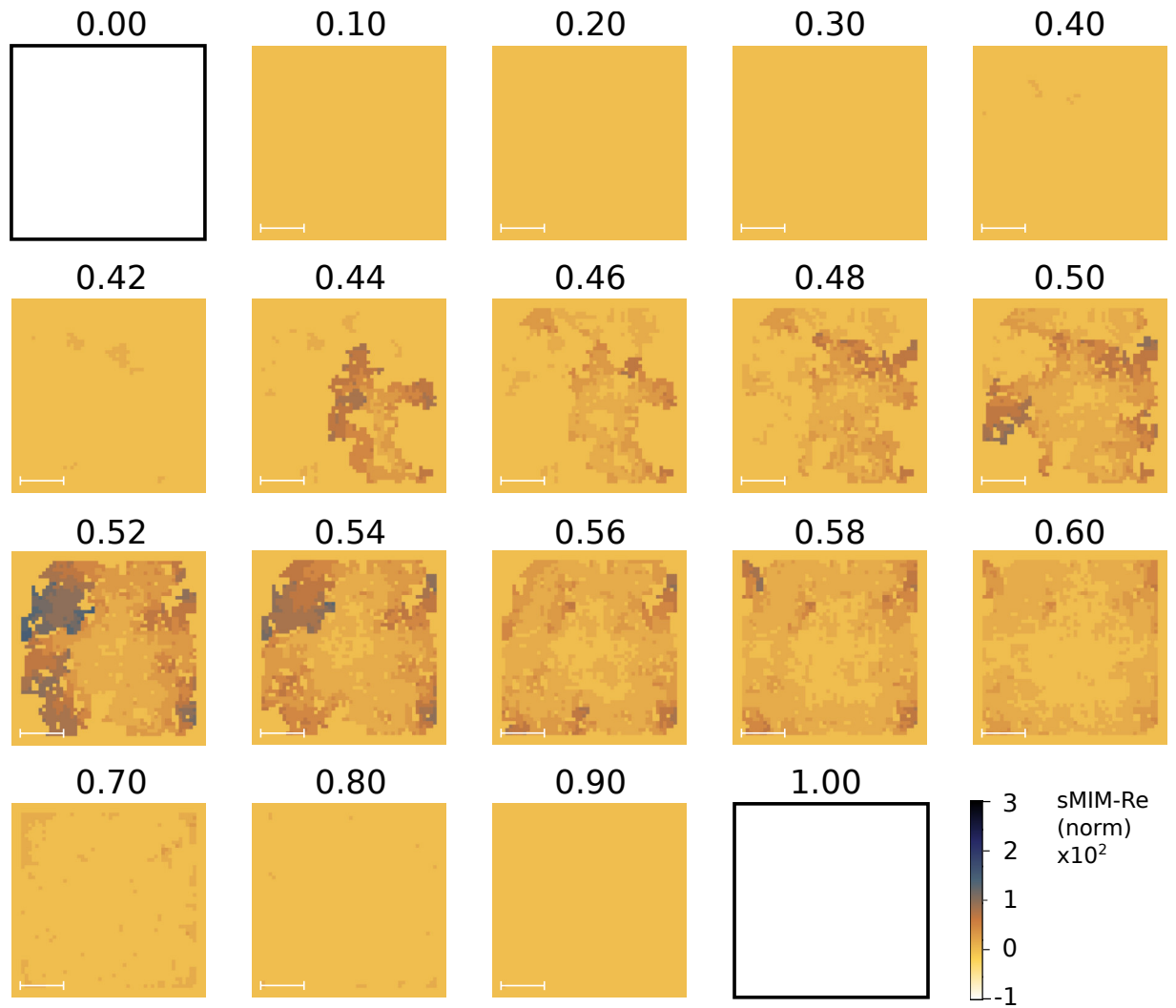


FIG. S12. Aluminum - sMIM-Re: Model calculations.

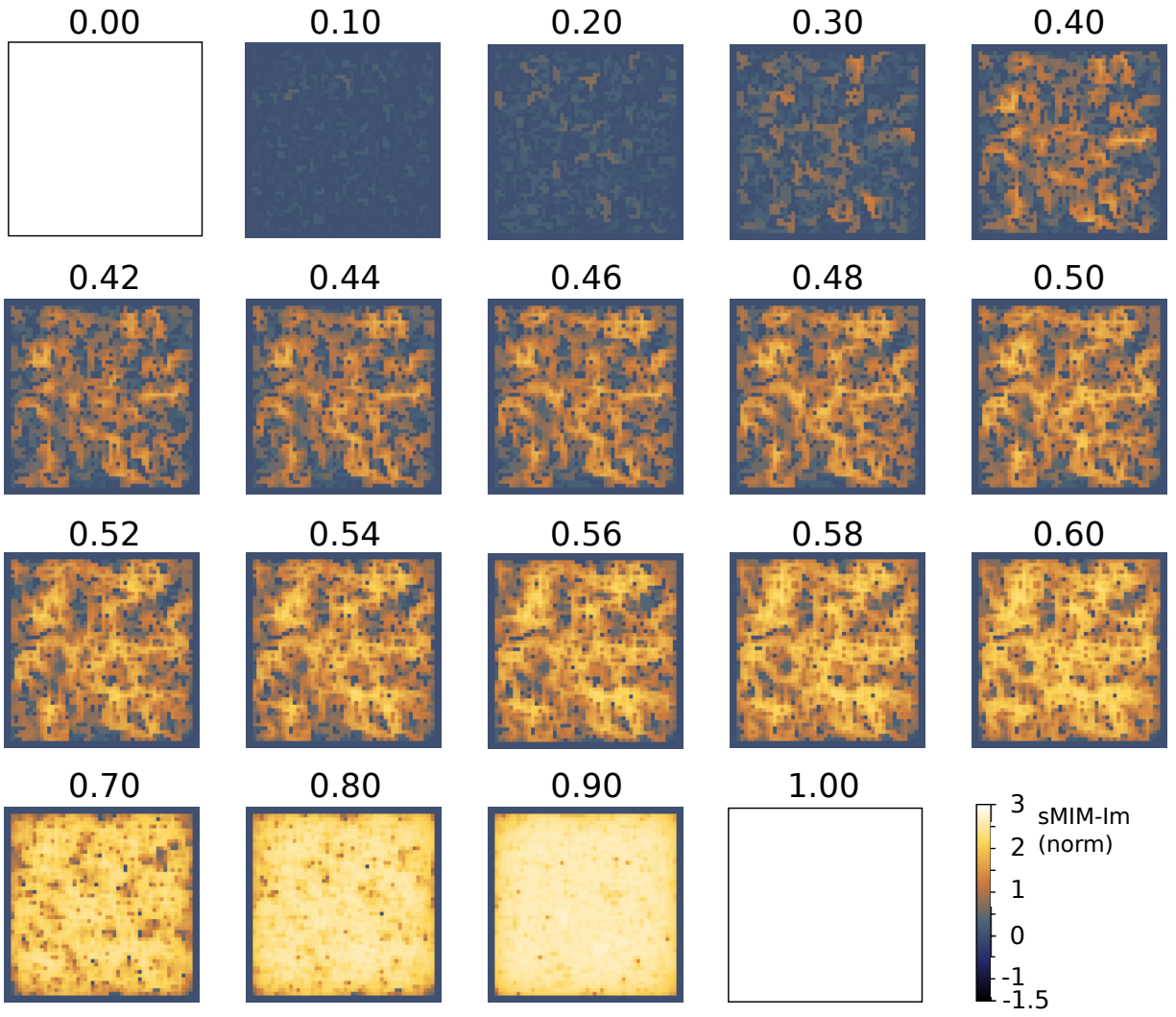


FIG. S13. NbTiN - sMIM-Im: Model calculations.

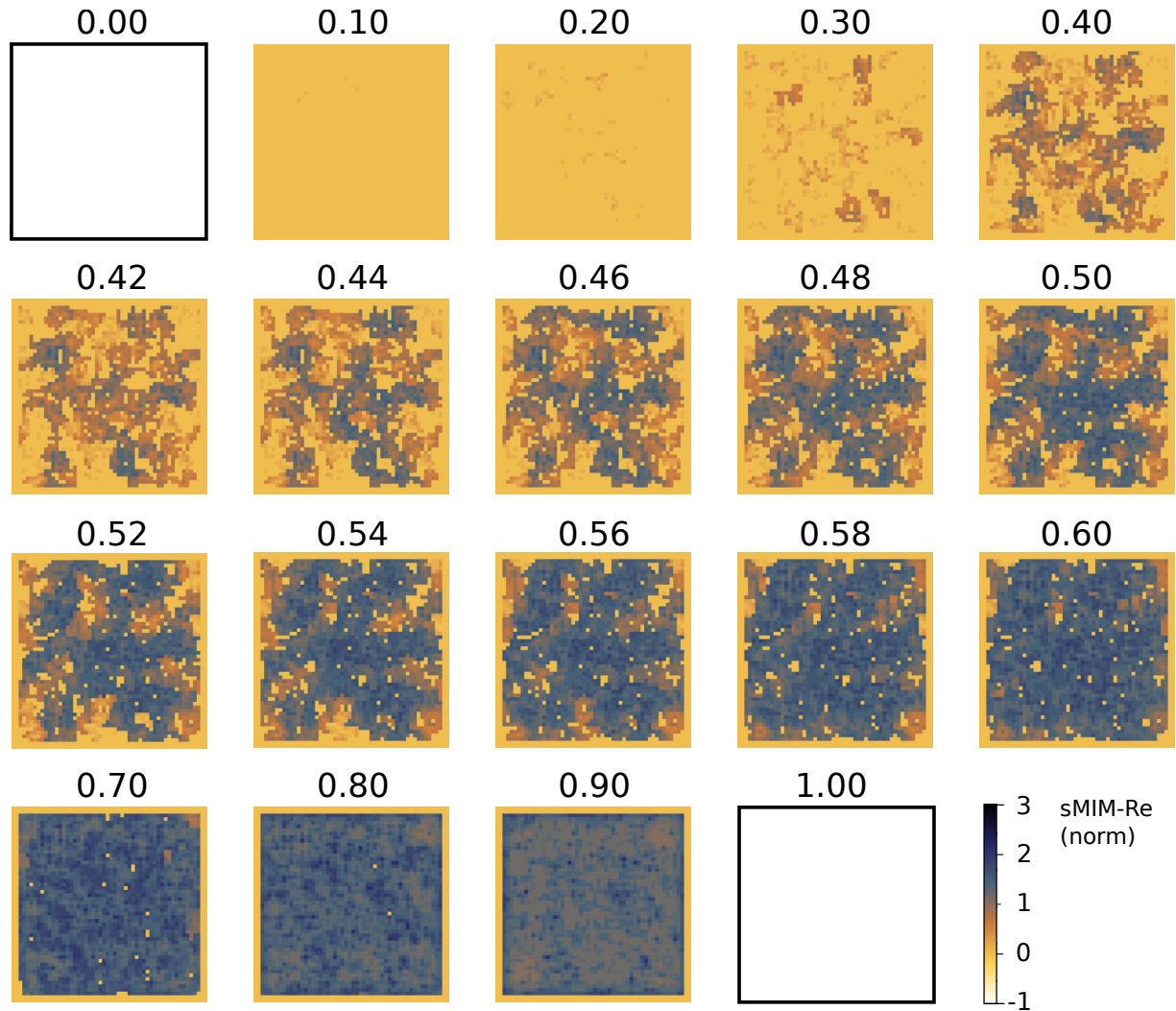


FIG. S14. NbTiN - sMIM-Re: Model calculations.

* h.r.thierschmann@tudelft.nl

- [1] D. Nečas and P. Klapetek, Gwyddion: an open-source software for SPM data analysis, *Open Physics* **10**, 181 (2012).
- [2] D. M. Pozar, *Microwave engineering* (John Wiley & Sons, 2009).
- [3] G. Jouve, C. Severac, and S. Cantacuzene, XPS study of NbN and (NbTi) N superconducting coatings, *Thin Solid Films* **287**, 146 (1996).
- [4] P. Van Mieghem, K. Devriendt, and H. Cetinay, Pseudoinverse of the laplacian and best spreader node in a network, *Physical Review E* **96**, 032311 (2017).